

Directionally Modified Fluorophores for Super-Resolution Imaging of Target Enzymes: A Case Study with Carboxylesterases

Yan Jia, Jiayue Wang, Peng Li, Xiaochi Ma, and Keli Han*



Cite This: *J. Med. Chem.* 2021, 64, 16177–16186



Read Online

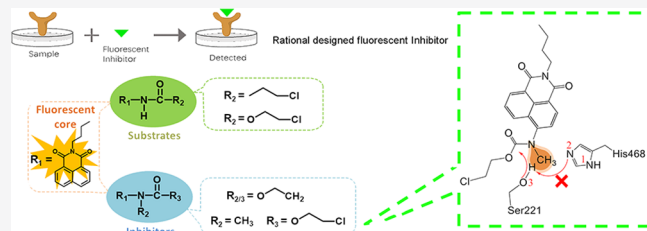
ACCESS |

Metrics & More

Article Recommendations

Supporting Information

ABSTRACT: In the need for improving the labeling quality of super-resolution imaging, multifarious fluorescent labeling strategies have sprang up. Among them, a small molecule inhibitor-probe (SMI-probe) shows its advancement in fine mapping due to its smaller size and its specific binding to a specific site. Herein, we report a novel protocol of mechanism-guided directional modification of fluorophores into fluorescent inhibitors for enzyme targeting, which could half the size of the SMI-probe. To confirm the feasibility of the strategy, carboxylesterase (hCE) inhibitors are designed and developed. Among the constructed molecule candidates, NIC-4 inhibited both isoforms of hCE1 and hCE2, with IC_{50} values of 4.56 and 4.11 μM . The CE-targeting specificity of NIC-4 was confirmed by colocalizing with an immunofluorescent probe in fixed-cell confocal imaging. Moreover, NIC-4 was used in live-cell super-resolution microscopy, which indicates dotlike structures instead of the larger staining with the immunofluorescent probe. Moreover, it enables the real-time tracking of dynamic flow of carboxylesterases in live cells.



INTRODUCTION

Rapid developments in molecular biology, organic chemistry, and materials sciences have led to multifarious fluorescent labeling strategies for protein imaging.^{1–4} Moreover, as the observation of cellular proteins is beyond the optical diffraction limit, super-resolution imaging techniques have come of age.^{5,6} In the field of super-resolution imaging of target proteins, the labeling characteristic of fluorescent probes is an essential factor for achieving the final high-quality images.⁷ For the targeting strategy (Figure 1A), the use of specific antibodies is the most conventional method. This strategy requires high-quality primary antibody and is usually restricted in scope, as working in permeabilized cells or with extracellular proteins.⁸ Moreover, a secondary-antibody-bound primary antibody or immunofluorescence-labeled primary antibody is always too large to cause a linkage error and low labeling density.⁹ Another commonly used strategy is the application of fluorescent transfection labeling. The fusion of a fluorescent protein would carry a fluorescent core, or the specific tag of a target protein would bind to a free fluorescent group and thus light up the target protein.⁸ The genetic recombinant technology requires miscellaneous transfection and/or transgenic procedures. Furthermore, the inherent functions of the targeted protein would be disturbed by the gene recombination process, and the overexpression or low expression of targeted gene could result in unreal imaging of the target protein.^{10,11}

These years, versatile approaches have been developed to approve the labeling quality and simplify the methodology; e.g., a relatively small fragment of antigen binding is selected in

fluorescence imaging. Nanobodies¹² and aptamers¹³ as novel small fluorescent labels have been applied in super-resolution imaging; however, the size is not small enough. Small molecule inhibitors conjugated with appropriate dyes (SMI-probe)¹⁴ appear as an ideal alternative to form small fluorescent labels. Due to the reduced steric hindrance between each other, smaller fluorescent labels can label denser than the corresponding antibody probe, with the morphology of labeling clusters smaller and more regular than the natural ligand.^{9,15}

Chemically reactive fluorescent dyes have been used for in vitro labeling of amine groups or thiol groups in proteins,^{16,17} and diverse derivatives of fluorescent compounds recognize different macromolecules due to subtle alterations in the structure. Among them, some have the potential to serve as a catalytic inhibitor of a specific protein. Despite high-throughput screening from marvelous commercial dyes to identify a specific inhibitor, directional modification of fluorophores serves as an alternative approach in developing potential fluorescent labels. Rational design applied in computer/mechanism-aided methods provides a knowledge-driven approach that can yield valuable information about the

Received: August 19, 2021

Published: October 25, 2021



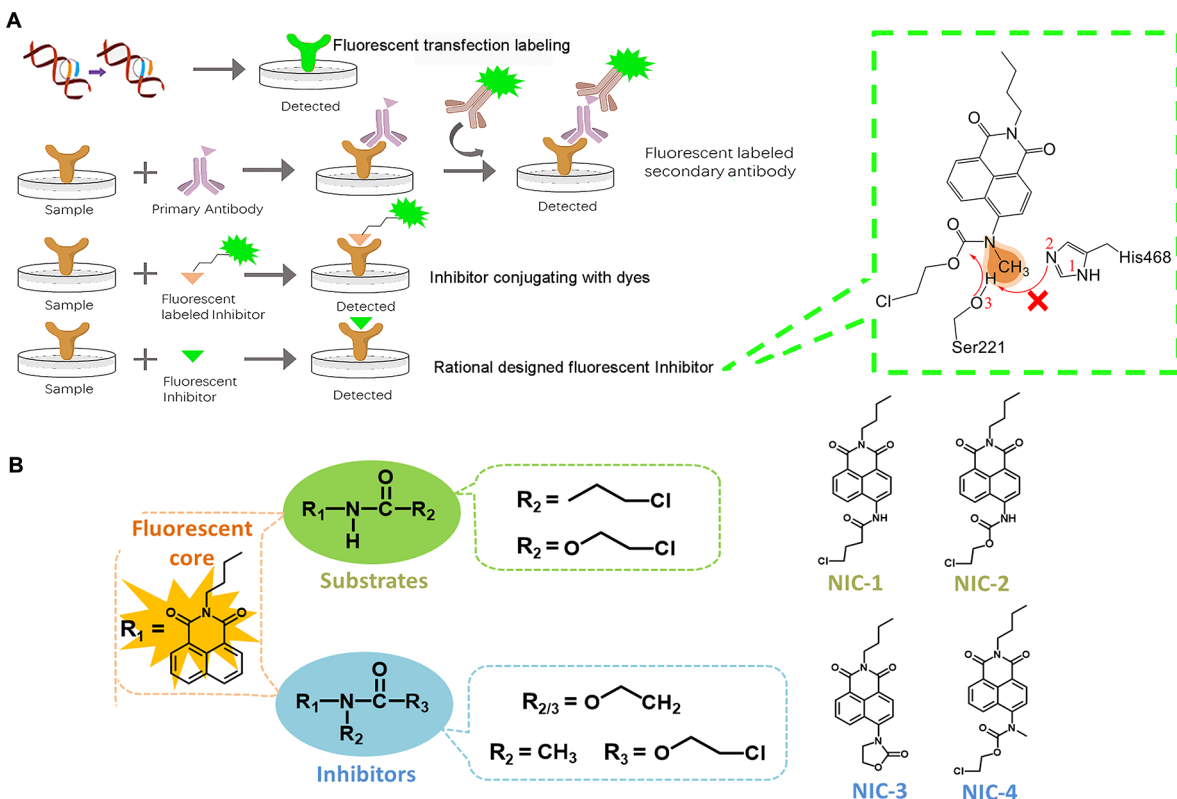


Figure 1. (A) Conventional fluorescent labeling strategy versus rationally designed strategy for fluorescent inhibitors introduced in this study, and the schematic diagram of detailed basis for the inhibition mechanism. (B) Structurally diversified carbamates designed and developed serve as inhibitors or substrates of hCEs in this study.

recognition/interaction patterns among inhibitors and proteins.¹⁸ The underlying mechanism would provide a basis for the direct transformation from a fluorophore to a fluorescent inhibitor. Compared with the SMI-probe, the size of the transformed dyes would be reduced by half in which process the labeling characteristic is highly likely to be improved.

Mammalian carboxylesterases (CEs) are important serine hydrolases playing major roles in the hydrolysis of endogenous esters (e.g., cholestry esters and triacylglycerols²⁰), xeno-biotics (e.g., cocaine and heroin²¹), and therapeutically active compounds (e.g., irinotecan²² and gemcitabine²³). CE plays key roles in biological processes. It participates in cholesterol homeostasis and fatty acid metabolism and thus affects lipid and glucose homeostasis.²⁴ Moreover, it plays pivotal roles in drug metabolism and is approved as a drug target by FDA. As a result, bioimaging and targeting of CE would aid in revealing its role in lipid/glucose homeostasis and in the treatment process of anticancer drugs.

Here, we report the pioneered design of a fluorescent inhibitor for CE and the successful use in structured illumination microscopy (SIM) imaging of CE. On the demand of high specificity toward CE, efforts have been made in data mining of reported substrates and inhibitors of CE, which include naturally occurring molecules and synthetic drug entities targeting and summing up the structure–activity relationship (SAR) of these ligands.^{25–30} Having found that modification of carbamate would be an important cut-in point, we developed NIC series with the same fluorescent scaffold and modified carbamate configurations (Figure 1B). Results showed that NIC-4 with methyl substitution of nitrogen in carbamate is an efficient inhibitor for both hCE isoforms. The

detailed mechanism study revealed that methyl substitution of nitrogen in carbamate effectively blocks the necessary proton transfer process, thus preventing the nucleophilic attack necessary for hydrolysis from happening. The targeting specificity of NIC-4 was then confirmed by colocalizing with an immunofluorescent probe in fixed cells, with high colocalization results achieved.

Moreover, NIC-4 was further used for live-cell super-resolution microscopy, which indicates fluorescence-labeled dotlike structures instead of the larger staining with an immunofluorescent probe. Furthermore, it was demonstrated to enable the real-time tracking of dynamic flow of CE in live cells.

RESULTS AND DISCUSSION

Human carboxylesterases (hCEs), a type of hydrolase responsible for endogenous metabolism of esters, serving as a major class of phase I drug-metabolizing enzymes, are approved as drug targets by FDA. There are two major isoforms of hCEs identified in humans, such as carboxylesterase 1 (hCE1) and carboxylesterase 2 (hCE2). They display a notable difference in tissue distribution and substrate preference.^{31,32} In addition to modulating lipid/glucose homeostasis, hCEs also participate in the activation of anticancer entities such as irinotecan and gemcitabine.^{19,23,33,34} Current reported inhibitors against hCEs encompass natural compounds like fatty acids,³⁵ flavonoids,²⁹ tanshinones,³⁶ and triterpenoids³⁷ and synthetic compounds like bisbenzene sulfonamides,²⁶ 1,2-diones,²⁸ trifluoroketones,³⁸ carbamates, etc. Among them, only the 1,2-dione moiety is well-elucidated as the classical functional group through covalently modifying

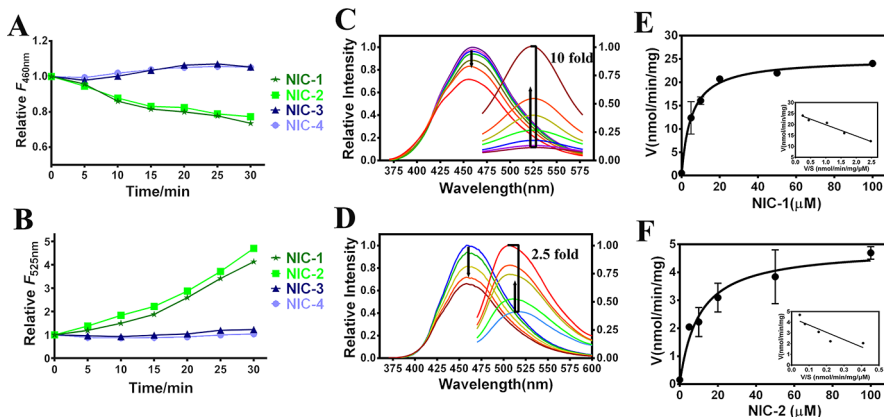


Figure 2. Evaluation of NIC series toward hCEs. Time-dependent relative fluorescence intensity change of NIC series toward hCE2, excited at (A) 460 nm wavelength and (B) 525 nm. Fluorescence spectral changes of (C) NIC-1 and (D) NIC-2 upon addition of varying concentrations of hCE2 during 30 min. Michaelis–Menten kinetic plot for (E) NIC-1 and (F) NIC-2 turnover toward hCE2; insets show the Eadie–Hofstee plot for each other. Profiling of the catalytic activity of hCE2 using NIC-1/2 was performed using the fluorescence intensity at 525 nm.

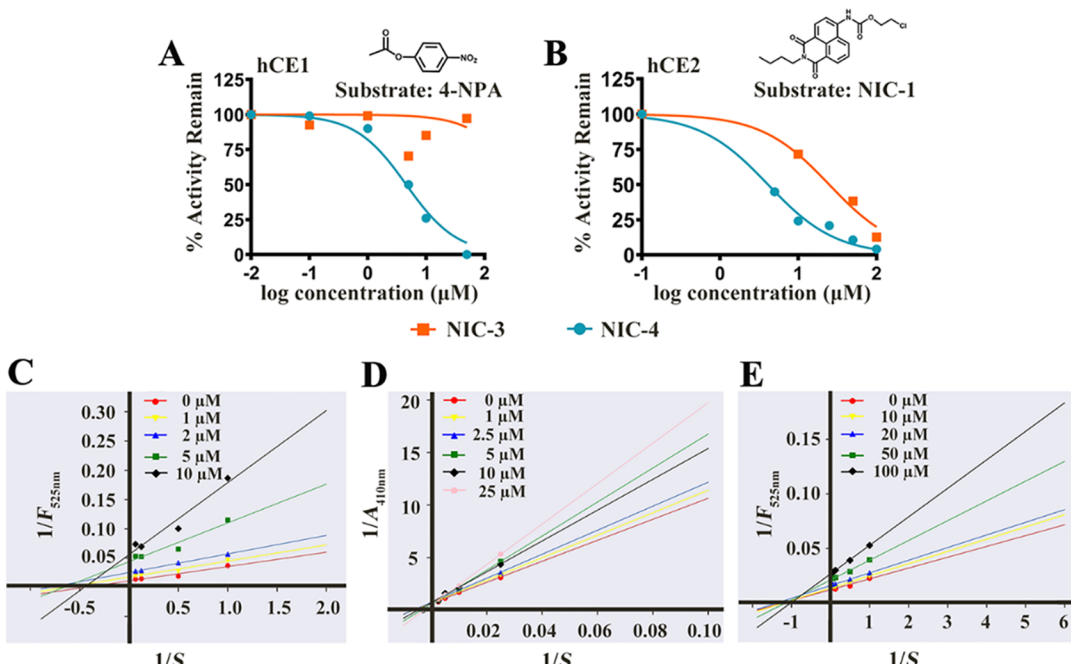


Figure 3. Inhibition properties of NIC series. Dose-inhibition curves of NIC-3 and NIC-4 on (A) 4-NPA hydrolysis in hCE1 and (B) NIC-1 hydrolysis in hCE2. Inhibition types for NIC-3/4 were defined by the Lineweaver–Burk analysis. Panel C for the inhibitory performance of NIC-3 against hCE2 in NIC-1 turnover. Panels D and E for hCE1-catalyzed 4-NPA turnover and hCE2-involved NIC-1 hydrolysis in the presence of NIC-4.

the key serine residue in the catalytic center of hCEs.³⁹ Apart from the 1,2-dione compounds, we have noticed the SAR between carbamate molecules and hCEs (Table S1). By simply categorizing the known active carbamate compounds into two groups, $R_1\text{-NH-CO-R}_2$ and $R_1\text{-NR}_2\text{-CO-R}_3$ (R_1 , R_2 , and R_3 in each structure type refer to nonhydrogen and varied substitution groups. R_1 in the former type is not equivalent to R_1 in the latter one, so as for R_2 and R_3), molecules with the former structure pattern tend to be substrates of hCEs with high specificities, such as the antitumor drug lidocaine⁴⁰ and recently reported hCE2 fluorescent probe NCEN.⁴¹ Meanwhile, compounds in the $R_1\text{NR}_2\text{COOR}_3$ configuration are more likely to exhibit inhibitory effects against hCEs, for example, the antidiarrheal medicine loperamide⁴² and

irreversible inhibitor of monoacyl-glycerol lipase JZL18432⁴³ (Table S1).

In this scenario, orientational transformation of fluorophores toward the $R_1\text{NR}_2\text{COOR}_3$ configuration would highly likely lead to the successful design of CE-specific fluorescent inhibitors. Therefore, we designed and synthesized a series of fluorescent molecules with a 1,8-naphthalimide fluorescent scaffold with different carbamate configurations. The 1,8-naphthalimide group was selected as a signal transducer because of its good photostability, high brightness, low phototoxicity, and ease of incorporation by an enzyme cavity, which would tolerate the increased laser intensity in SIM imaging. With the same fluorescent scaffold, the SAR effect of the carbamate difference would be enlarged and manifested. The construction of the fluorescent carbamate molecules was

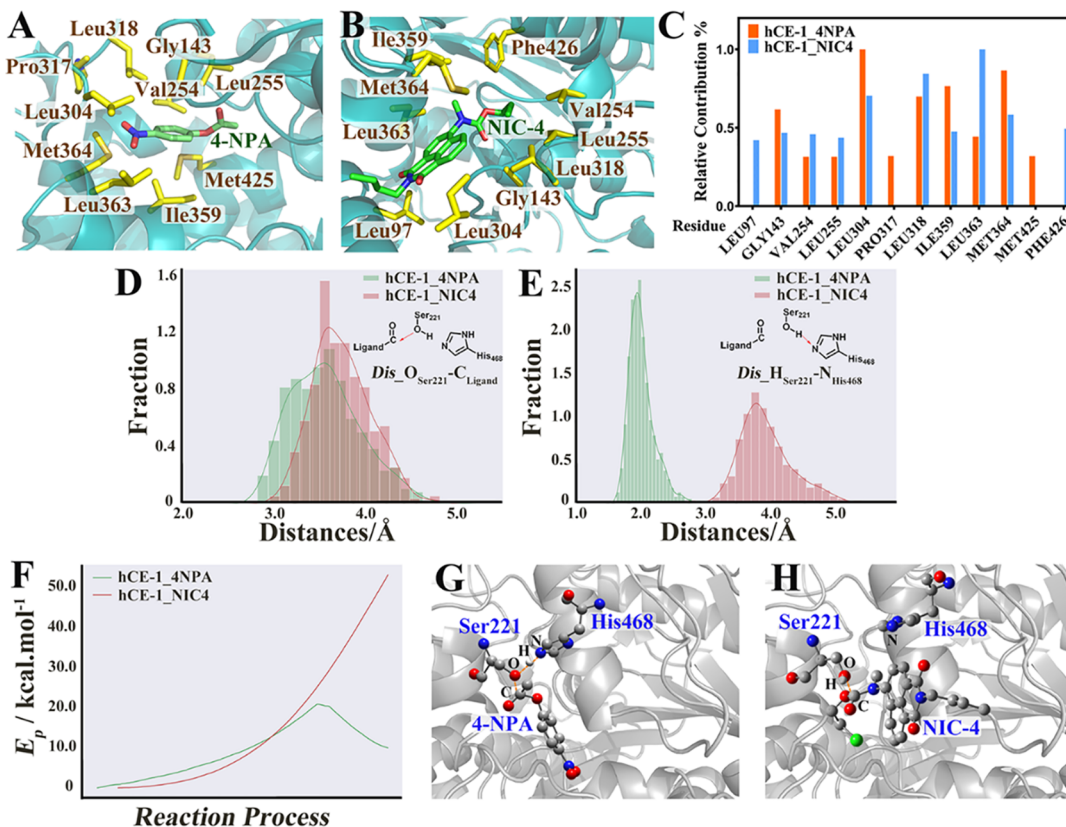


Figure 4. Mechanism study for NIC-4 inhibition originality against hCE1 in comparison with substrate 4-NPA. Interaction formats for (A) 4-NPA and (B) NIC-4 binding in the active site of hCE1. (C) Key residue spectra revealed from energy decomposition study for NIC-4 and 4-NPA interacting with hCE1. Key distance distribution measured from O_{Ser221} to C_{Ligand} corresponding to the nucleophilic attack process and from N_{His468} to H_{Ser221} representing the proton transfer process in NIC-4_hCE1 and 4-NPA_hCE1 systems sampled from 20 ns MD study is shown in panels D and E, respectively. The energy profile along with the nucleophilic attack from the hydroxyl group of Ser221 toward the carboxyl group of 4-NPA and the amide group of NIC-4 is presented in panel F. (G) Frame collected near the transition state in the 4-NPA_hCE1 system shows details in the catalytic process. (H) Frame retrieved at the same attacking distance as the 4-NPA_hCE1 system for the NIC-4_hCE1 system. Distribution pattern of distances from HSer221 to NHis468 ($Dis-H_{Ser221}-N_{His468}$).

executed according to the synthesis procedures described in Scheme S1. The compounds with the R_1NHCOR_2 structure pattern were named NIC-1 and NIC-2, while others with the $R_1NR_2COR_3$ moiety were labeled as NIC-3 and NIC-4 (Figure 1B). Their structures were fully characterized by 1H NMR, ^{13}C NMR, and HRMS spectral studies (Figures S2–S11). Fluorescence spectroscopy study of the NIC series showed that NIC molecules possess a similar maximum absorbance at 350 nm, while the maximum emission for NIC-1, NIC-2, and NIC-4 is 460 nm and its redshift to 470 nm for NIC-3 (Figure S12).

Evaluation of NIC Series toward hCEs. With the verified structure and specified maximum absorbance/emission wavelength for each NIC molecule, in vitro kinetic studies were carried out. Under physiological conditions ($pH = 7.4$; temperature = 37°C), the time profile of fluorescence intensities has been recorded for the NIC series coincubated with hCE1 and hCE2. In hCE1 systems, there was no obvious intensity alteration for all the NIC compounds. In hCE2 systems, the emission intensities at 460 nm have decreased for NIC-1 and NIC-2 (Figure 2A). In addition, an emission intensity increase has been observed at 525 nm for these two NIC molecules in the same systems (Figure 2B).

With reducing intensity recorded at 460 nm and fluorescence enhancement at 525 nm, hydrolysis of NIC-1/2 conducted by hCE2 is sure to happen (Figure 2C,D). The

behaviors of NIC-1/2 catalyzed by hCE2 were then carefully measured. Kinetically, both followed a typical Michaelis–Menten model (Figure 2E,F). K_m values for NIC-1 and NIC-2 were measured as 5.15 and $9.98 \mu\text{M}$, respectively. The V_{max} values were determined to be 25.0 and 4.9 nmol/min/mg , respectively. Compared with 4-nitrophenyl acetate (4-NPA), a commonly used substrate of hCEs, with measured K_m and V_{max} values of $\sim 170 \mu\text{M}$ and $0.72 \mu\text{mol/min/mg}$ for hCE233, respectively, our NIC molecules possess ideal properties in sensitivity and catalytic efficiency. We further tested the catalytic preferences of NIC-1/2 toward a panel of human esterases and plasma proteins. Results showed that NIC-1/2 can be hydrolyzed by hCE2 with high specificity (Figure S14). In summary, these results confirm our hypothesis in part as carbamate with the configuration of $R_1-\text{NH}-\text{CO}-R_2$ serves as the substrate of hCEs (hCE2 for NIC-1/2).

In contrast with NIC-1/2, NIC-3/4 showed responses toward neither hCE1 nor hCE2 (Figure 2A,B). Subsequently, their potential inhibitory effects against hCEs were investigated. Having known that NIC-1/2 molecules are sensitive and efficient agents in activity determination of hCE2, especially NIC-1 with lower K_m and larger turnover rates, we used NIC-1 here as the substrate in the hCE2 profiling. 4-NPA, the typical substrate for hCE1, was used in the corresponding analysis. Revealed from the steady-state kinetic experiments, the catalytic efficiencies of both hCEs have been

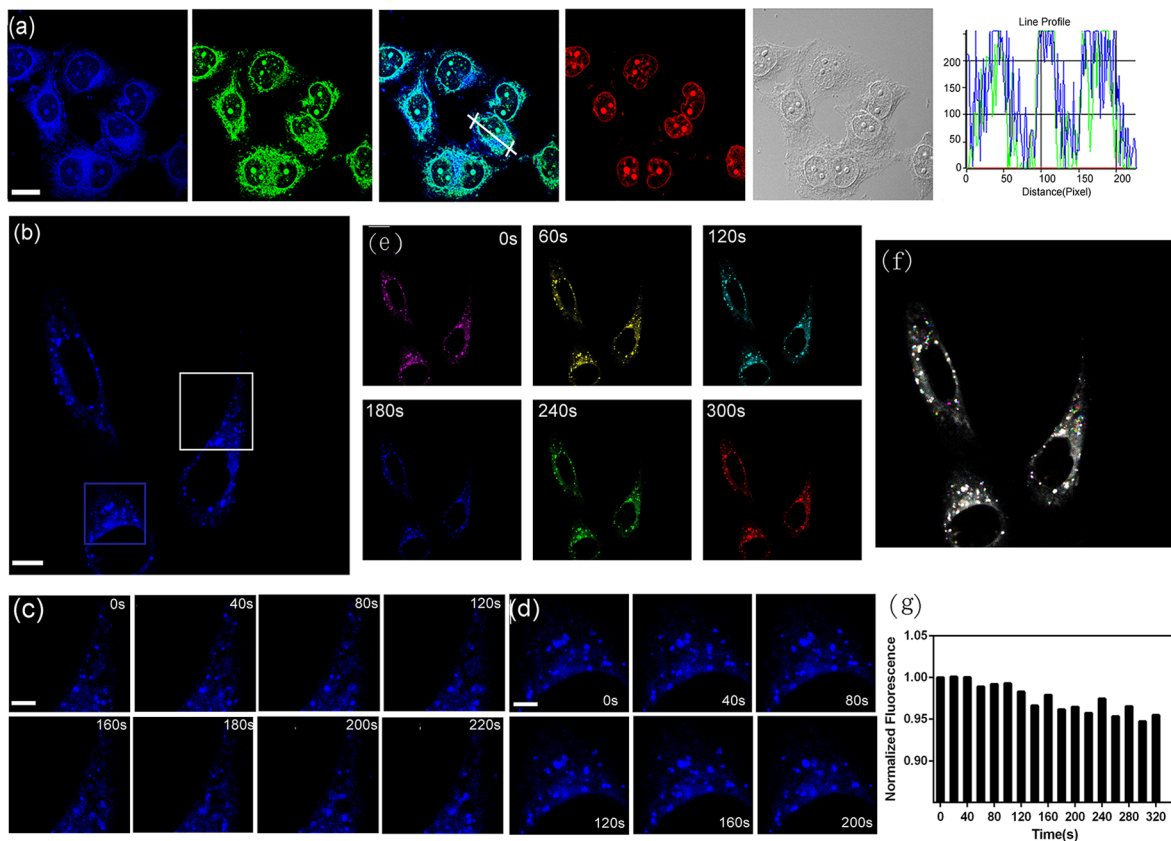


Figure 5. Orthotopic fluorescent labeling performance of NIC-4 targeting hCE1 in the HL7402 cell line. (a) The confocal imaging results for NIC-4 ($\lambda_{\text{ex}} = 405 \text{ nm}$, images collected from a 425–475 nm blue channel) costained with a commercially available antibody fluorescent probe targeting specifically hCE1 ($\lambda_{\text{ex}} = 488 \text{ nm}$, images collected from a 500–600 nm green channel). Regions of colocalization appeared in cyan. Nuclei were stained with Nucview Red Live ($\lambda_{\text{ex}} = 635 \text{ nm}$ and images were collected through a 647–755 nm red window) and appeared in red. Scalebar: 20 μm . (b) Super-resolution imaging (SIM imaging) of hCE1 in whole live 7402 cells stained with NIC-4. Scale bar: 10 μm . (c and d) Time-lapse SIM images of different areas of hCE1 movement in boxed regions in b, representatively. For the time-lapse images, the time interval between each SIM image was set to 20 s with a course of 4 min. Scalebar: 5 μm in Figure 5c and 4 μm in Figure 5d. (e) Time-colored images of (b). (f) Merge channel of the time-colored imaging results shown in (e). (g) Fluorescence intensity of NIC-4 in cells under SIM illuminations during the whole imaging process.

reduced along with the increase of NIC-4 concentration (Figure 3A,B, the blue line). Measured IC₅₀ values for NIC-4 against hCE1 and hCE2 were 4.56 and 4.11 μM , respectively. On the other hand, NIC-3 showed no obvious inhibitory effects on hCE1, while it exhibited mild effects against hCE2, with a measured IC₅₀ value of 25.08 μM . The Lineweaver–Burk plots were used to further investigate the inhibition type. With varied inhibitor concentrations, the catalytic efficiencies defined in the form of product absorption (4-NPA, at 410 nm)/fluorescent emission (NIC-3/4 at 525 nm) intensity (reciprocal) were plotted against the substrate concentration (reciprocal). As shown in Figure 3C, NIC-3 exhibited a noncompetitive inhibitory effect in hCE2-catalyzed NIC-1 turnover, as the plotted lines intersected at the X axis. The inhibition type was more evitable when it comes to NIC-4-involved hCE catalysis. Revealed from Figure 3D,E, the intersection points approaching the Y axis for hCE1-catalyzed 4-NPA turnover indicated that NIC-4 is a competitive inhibitor with 4-NPA in hCE1 catalysis, while the intersection points approaching the X axis for hCE2-catalyzed NIC-1 turnover showed that it is a noncompetitive inhibitor in this situation. Taken together, the results confirmed our proposed theorem that carbamate with configurations of R₁-NR₂-CO-R₃ serves as the inhibitor of hCEs. In addition, the star molecule

NIC-4 is an ideal and moderate inhibitor for hCEs with an identical competitive type for each isoform. The difference between hCE isoforms from inhibition type analysis further revealed their substrate preferences.³⁰

Mechanism Study of the Basis for Inhibition Originality. As the subtle alteration of carbamate configuration results in evident changes in the catalytic activity, the mechanism behind the SAR attracts our attention. In consideration of the known crystal structure for hCE1 and the inhibition type identified above that helps to locate the potential binding site of NIC-4, we carried out the mechanism study of NIC-4 in comparison with substrate 4-NPA targeting hCE1. After model selection with the calculated binding energy from molecular dynamics simulation, the ligand–protein interaction modes for NIC-4_hCE1 and 4-NPA_hCE1 have been carefully defined (Figure 4A,B). From binding energy decomposition analysis, key residues that help NIC-4 and 4-NPA binding with hCE1 have a large overlap. (Figure 4C) The key residues for NIC-4 binding have a wider range in distribution than 4-NPA because of the obvious bulk structure. Such results indicate that, compared with the substrate, NIC-4 has no evitable differentiation in the interaction format with hCE1. We thus dug deeper and sampled the ligand–protein interaction on a time scale of 20 ns.

Previously reported studies have confirmed the significance of Ser221 and His468 in the hCE1 reaction, of which the former residue is the nucleophilic attack center toward substrates.^{18,28,37} We sampled the distribution of key distance involved in the initial hydrolysis reaction. As shown in Figure 4D, the distance from OSer221 to CLigand (Dis-OSer221-CLigand) corresponding to the nucleophilic attack process has the same distribution pattern for both systems. The peak value collected at 3.5~3.7 Å indicates that such a distribution pattern would be favored for both systems to initiate the nucleophilic attack from Ser221. Things are different when it comes to the distribution pattern of distance from HSer221 to NHis468 (Dis-HSer221_NHis468). As can be seen from Figure 4E, the distribution of Dis-NHis468_HSer221 for the 4-NPA_hCE1 system is narrow and peaks at 2.0 Å, which is within the ideal range for proton transfer from Ser221 to His468.

On the other hand, such proton transfer would not happen in the NIC-4_hCE1 system since the distribution pattern for Dis-NHis468_HSer221 fluctuates around 3.7 Å. Further steered MD (sMD) study reproduced the reaction possibility, as the nucleophilic attack from the hydroxyl group of Ser221 would certainly happen in the 4-NPA_hCE1 system with the energy barrier estimated to be around 20 kcal/mol. The other system, however, would not go through the same hydrolysis process, since there is no barrier (Figure 4F). Conformation retrieved near the transition state from the 4-NPA_hCE1 system reveals that the proton transfer process is necessary for the hydrolysis reaction (Figure 4G). In the other system, we collected frames at the same attack distance as in the 4-NPA_hCE1 system. Results presented in Figure 4H showed no sign for proton transfer from Ser221 to His468, as the methyl group near the potential nucleophilic center of NIC-4 hinders the transfer path and forces the hydroxyl group of Ser221 to orient away from the imidazole group of His468. In summary, the aforementioned study helps to explain the mechanism of NIC-4 being an ideal inhibitor of hCE1. It mimics the interaction pattern of the classic substrate to benefit enzyme binding but hinders the necessary proton transfer process by methyl substitution of nitrogen in carbamate, thus preventing the nucleophilic attack from happening. In this way, a competitive inhibition is observed in NIC-4-inhibited 4-NPA turnover by hCE1.

Orthotopic Labeling Performance of the Fluorescent Inhibitor. Having synthesized with the proposed scheme, identified the inhibitory properties, and modeled the mechanism of inhibition originality, NIC-4 has been placed with great expectations to be an ideal candidate for hCE imaging. We thus tested its performance in orthotopic hCE labeling from HL7402 cells. Before the bioimaging study, the toxicity of the probe against HL7402 cells was investigated by the CCK-8 assay. After 48 h incubation, no significant toxicity has been observed (Figure S16, details for cell preparation, cell viability test, and cell imaging are provided in the Supporting Information). We next sought to carry out wash-free fluorescence labeling of intracellular proteins in fixed cells and compare with an immunofluorescent method. As shown in Figure 5a, after incubation with 2 μM NIC-4 for 20 min, HL7402 cells were directly imaged without washout processes, with strong blue fluorescence (the wavelength ranges from 420–480 nm) observed in the cytoplasm. Costaining with hCE1-specific monoclonal antibody (antiliver CE1 conjugated with IgG (H + L) Cross-Adsorbed Secondary Antibody DyLight 488) and Nucview Red Live validated that NIC-4

visualized the localization of hCE1 in the cytoplasm (Figure 5a). Regions of colocalization in the appearance of cyan were estimated with an overlapping coefficient as high as 0.749 (Table S2). Thus, the results demonstrated that NIC-4 could be applied in hCE1 visualization without fussy washing steps required in the immunostaining process.

As NIC-2 serves as an activity-based probe for hCEs, the imaging property of NIC-2 is also tested in comparison with NIC-4. As shown in Figure S17, after incubating for 20 min, NIC-2 suggests strong blue fluorescence (420–480 nm) and green fluorescence (500–600 nm), suggesting product information. In the magnifying perspective (Figure S17, bottom panel), the large staining of NIC-2 in the blue and green channel tends to behave like endoplasmic network imaging. Under the same irradiation, NIC-4 indicates blue fluorescence (420–480 nm) alone, and the staining is more likely to be a collection and accumulation of scattered dots. This reveals the different interaction pattern between NIC-2-hCE and NIC-4-hCE. NIC-2 and its product distributed uniform in the cytoplasm, while NIC-4 as the inhibitor binds to the target enzyme more stably and has the potential for long-term observation.

The localizing effect of the hCE fluorescent sensor is closely related to the characteristics of the fluorescent scaffold. hCEs are reported to be a protein spread in the cytoplasm, and many suggest that they locate on the endoplasmic reticulum,^{44,45} while others suggest dotlike structures in the cytoplasm using a fluorescent sensor^{41,46} and immunostaining reagent.⁴⁷ The labeling characteristic is better observed using super-resolution imaging. As a result, we next sought to carry out NIC-4 staining using SIM imaging to obtain precise marking of hCE. By addition of 2 μM NIC-4, we observed large area of staining in the cytoplasm (Figures 5a and S17 and S20) without any specific direction. Therefore, we next use low concentrations of NIC-4 (0.5 μM) to capture the fine structure of hCE marking. Consequently, low-concentration staining indicates smaller amounts of scattered dots in the cytoplasm in contrast to the confocal imaging (Figures 5b-d and S20). Compared with immunofluorescent images showing a negligible green background, NIC-4 staining SIM images suggest clear fluorescence at specific positions.

As naphthalimide, the scaffold of NIC-4, was reported in significant photo bleach resistance and would be an ideal material for long-term SIM imaging, the phototoxicity and photostability of NIC-4 were tested. As acute photo toxicity would cause evident morphological changes in living cells, here we evaluated the morphological performance of HL-7402 cells labeled by NIC-4 during continuous SIM illumination. While the cells were irradiated with a 405 nm SIM laser for 18 times, each for 90 ms, the cell morphology remains basically unchanged (Figure S18). Of the 18 SIM images, we selected and colored 6, which were obtained every 60 s in different channels (Figure 5e) and merged them to generate Figure 5f. While white areas of Figure 5f indicate the minimal changes of cells, the colorful dots depict the subtle movement of the target protein. We also evaluated the photobleaching properties of NIC-4 marked on hCEs during the same imaging process. As shown in Figure 5g, after 18 consecutive scans, the fluorescence intensity remains at 95% of the initial value. Due to the good brightness, photostability, and excellent fluorogenic properties for no-wash labeling, probe NIC-4 can not only achieve long-term protein observation but also facilitate the observation of the fast protein dynamic processes.

In summary, NIC-4 labeled on hCEs did not significantly affect cell morphology and function. With almost no cellular toxicity, low phototoxicity, excellent antibleaching ability, and ideal specificity equivalent to the immunofluorescence probe, it remains an excellent hCE marker and has great potential in the field of long-term super-resolution imaging. Moreover, the practical easy-to-handle property and delicate design strategy we proposed here would shed light on the future development of the protein-targeting method.

CONCLUSIONS

In the need of a cost-effective and simplified method with an improved labeling characteristic for super-resolution imaging, here we report a novel labeling strategy by transforming fluorophores directly into fluorescent inhibitors guided by the data mining and mechanism study. Taking CE as an example, having found that substitution at the carbamate group would hinder the proton transfer process, thus terminating the nucleophilic attack and inhibiting the hCE1-catalyzed substrate turnover, we rebuild the fluorophore by modifying the substitution of the carbamate. The star molecule NIC-4 turned out to show inhibitory effects on both isoforms hCE-1 and hCE-2. By comparing with NIC-2 and the immunofluorescent probe, NIC-4 is superior in hCE marking in living cells with great potential of long-term super-resolution imaging. To our knowledge, this is the first reported rationally designed fluorescent inhibitor used in CE targeting. The knowledge-driven directional transformation of fluorophores would serve as a novel, simplified, and convenient protein labeling strategy, which would serve as a good starting point for a more convenient, less expensive, and easily performed strategy toward the wider scope of enzymes shortly soon.

EXPERIMENTAL SECTION

Detailed Synthetic Procedures of NIC-1. Compound 1 (0.5 g) (1.86 mmol) was suspended in 20 mL of 1,4-dioxane and 4-chlorobutyryl chloride (206 μ L) (1.86 mmol), and EtN₃ (774 μ L, 5.58 mmol) was added. The mixture was refluxed for several hours, and the reaction was monitored by thin-layer chromatography (TLC). After the complete reaction, the mixture was cooled to room temperature, and the solvent was evaporated on a rotary evaporator until dry. The solid was purified by column chromatography on a silica gel using dichloromethane. Yield: (0.50 g, 72% yield). LC-MS (API-ES): *m/z* C₂₀H₂₁ClN₂O₃ [M + H⁺] 372.13, found 373.13. ¹HNMR (400 MHz, CHLOROFORM-D) δ (ppm): δ = 8.62 (d, 1H, *J* = 7.2 Hz), 8.58 (d, 1H, *J* = 8.4 Hz), 8.38 (d, 1H, *J* = 8.0 Hz), 8.18 (d, 1H, *J* = 8.4 Hz), 7.93 (s, 1H), 7.77 (t, 1H), 4.17 (t, 2H, *J* = 5.2 Hz), 3.74 (t, 2H, *J* = 7.6 Hz), 2.80 (t, 2H, *J* = 5.6 Hz), 2.30 (m, 2H, *J* = 5.6 Hz), 1.70 (m, 2H), 1.46 (m, 2H), 0.98 (t, 3H, *J* = 8.0 Hz). Purity is >95%.

Detailed Synthetic Procedures of NIC-2. Compound 2 (0.5 g) (1.86 mmol) was suspended in 20 mL of 1,4-dioxane and 2-chloroethyl chloroformate (232 μ L) (1.86 mmol), and EtN₃ (774 μ L, 5.58 mmol) was added. The mixture was refluxed for several hours, and the reaction was monitored by TLC. After the complete reaction, the mixture was cooled to room temperature, and the solvent was evaporated on a rotary evaporator until dry. The solid was purified by column chromatography on a silica gel using dichloromethane. Yield: (0.55 g, 79% yield). LC-MS (API-ES): *m/z* C₁₉H₁₉ClN₂O₄ [M + H⁺] 375.10, found 375.10. ¹HNMR (400 MHz, CHLOROFORM-D) δ (ppm): δ = 8.64 (d, 1H, *J* = 7.2 Hz), 8.60 (d, 1H, *J* = 8.4 Hz), 8.34 (d, 1H, *J* = 8.0 Hz), 8.19 (d, 1H, *J* = 8.4 Hz), 7.80 (t, 1H, *J* = 7.6 Hz), 7.49 (s, 1H), 4.55 (t, 2H, *J* = 5.2 Hz), 4.18 (t, 2H, *J* = 7.6 Hz), 3.81 (t, 2H, *J* = 5.6 Hz), 1.72 (m, 2H), 1.46 (m, 2H), 0.98 (t, 3H, *J* = 8.0 Hz). Purity is >95%.

Detailed Synthetic Procedures of NIC-3. NIC-2 (0.1 g) (0.26 mmol) was suspended in 5 mL of methanol, and tetramethylguanidine (65 μ L) was added and mixed for 30 min. The reaction was monitored by TLC. After the complete reaction, the solution was evaporated to dry, and the solid was purified by column chromatography on a silica gel using dichloromethane. Yield: (0.09 g, 95% yield). LC-MS (API-ES): *m/z* C₁₉H₁₈N₂O₄ [M + H⁺] 339.13, found 339.13. ¹HNMR (400 MHz, chloroform-d) δ (ppm): δ = 8.64 (d, 1H, *J* = 7.2 Hz), 8.61 (d, 1H, *J* = 8.0 Hz), 8.28 (d, 1H, *J* = 8.6 Hz), 7.80 (t, 1H, *J* = 7.8 Hz), 7.69 (d, 1H, *J* = 7.6 Hz), 4.71 (t, 2H, *J* = 8.2 Hz), 4.20 (m, 4H), 1.72 (m, 2H), 1.45 (m, 2H), 0.98 (t, 3H, *J* = 7.2 Hz). ¹³CNMR (100 MHz, chloroform-d) δ (ppm): 163.90, 163.44, 156.59, 140.13, 131.11, 129.32, 127.78, 127.36, 123.35, 123.29, 122.22, 62.77, 48.68, 40.34, 30.18, 20.37, 13.85. Purity is >95%.

Detailed Synthetic Procedures of NIC-4. Compound 3 (0.524 g) (1.86 mmol) was suspended in 20 mL of 1,4-dioxane and 4-chlorobutyryl chloride (206 μ L) (1.86 mmol), and EtN₃ (774 μ L, 5.58 mmol) was added. The mixture was refluxed for several hours, and the reaction was monitored by TLC. After the complete reaction, the mixture was cooled to room temperature, and the solvent was evaporated on a rotary evaporator until dry. The solid was purified by column chromatography on a silica gel using dichloromethane. Yield: (0.469 g, 65% yield). LC-MS (API-ES): *m/z* C₂₀H₂₁ClN₂O₃ [M + H⁺] 389.12, found 389.12. ¹HNMR (400 MHz, chloroform-D) δ (ppm): δ = 8.63 (m, 2H, *J* = 7.2 Hz), 8.18 (d, 1H, *J* = 8.4 Hz), 7.80 (d, 1H, *J* = 8.0 Hz), 7.63 (d, 1H, *J* = 8.4 Hz), 4.43 (t, 2H), 4.17 (t, 2H), 3.94 (t, 2H, *J* = 5.2 Hz), 3.52 (s, 3H), 2.80 (t, 2H, *J* = 5.6 Hz), 1.72 (m, 2H), 1.46 (m, 2H), 0.98 (t, 3H, *J* = 8.0 Hz). Purity is >95%.

Enzyme Kinetic Assay. The reaction was initiated by adding NICs in 100% DMSO (2 μ L) to preincubated hCEs (198 μ L, 0.1 mg/mL, phosphate buffer solution, PH = 7.4), at a final concentration of 0.1 to 50 μ M. The reaction between NIC and hCEs took place at 37 °C. Incubation proceeded for 10 min, and the emission intensity at 530 nm was immediately detected using a Thermo Scientific Varioskan Flash Multimode Reader (Thermo, USA).

Enzyme Inhibition Study. Inhibition experiments were performed in a total volume of 200 μ L of PBS containing 0.1 mg/mL hCEs, 10 μ M NIC-1/200 μ M 4-NPA, and various inhibitors (from 0.1 to 100 μ M). Fluorescence emission (absorbance) from protein-free samples containing the substrate and potential inhibitors was subtracted as background. A decrease in fluorescence (absorbance), indicating inhibition of enzyme activity, was observed after 10 min of incubation with excitation at 450 nm and emission at 520 nm (absorbance at 405 nm) on a Thermo Scientific Varioskan Flash Multimode Reader (Thermo, USA).

Computational Details for the Mechanism Study. The initial ternary structure of human carboxylesterase-1 (hCE1) was obtained from the PDB database with entry code 2H7C.⁴⁸ The chain A representing monomer was used for simulation. Structure information without a ligand was used as the receptor for the molecular docking and apo-system for blank control. The protonation states of titratable residues were carefully assigned according to the calculated pK_a values by the PDB2PQR online server.⁴⁹ For histidine-involved protonation definition, His468 in the catalytic center was protonated at the δ position. Afterward, hydrogen atoms were added and optimized using the casual force field ff14SB⁵⁰ in the Amber16 package.⁵¹ Geometrical optimization for studied ligands 4-NPA and NIC-4 was carried out at the level of B3LYP theory^{52–54} with the 6-311 + G(2d,p)⁵⁵ basis set in Gaussian 16 A03.⁵⁶ Parameters of the bonds, angles, dihedrals, and van der Waals of the ligand were then fitted based on restrained electrostatic potential (RESP) charges in the force field of generalized Amber force field embedded in the Amber16 package. The Auto-Dock Vina program⁵⁷ and the default parameters were used to obtain a series of conformations with 4-NPA and NIC-4 binding to hCE1. The docking box was centered by the Ser221–Glu354–His468 catalytic triad and set to embrace the whole cavity. From the initial docking performance, nine binding models for each ligand were generated and used as the starting conformation set molecular dynamics (MD) simulation. The binding models of 4-NPA_hCE1

and NIC-4_hCE1 were fully solvated in the truncated-orthorhombic-shaped boxes. The solvation thickness is at least 10 Å, and the TIP3P model⁵⁸ was applied to describe the water molecules. Sodium ions were added to ensure the neutrality. The solvated complexes were relaxed with minimization run to release bad contacts and heated with a 200 picosecond (ps) procedure to reach 300 K. Before the production run, another 200 ps simulation aiming at stretching hydrogen and side chains of the system was executed. The production stage of the MD process ran under isothermal-isobaric ensemble conditions from which the last 1 ns trajectory was used for binding energy calculation. A binding system with the lowest calculated energy value was selected as the representing model for 4-NPA/NIC-4_hCE1. The elongated 20 ns simulation for each of the selected ligand binding models based on which the ligand–protein interaction analysis would be carried out was performed. The final 20 ns trajectories were used for ligand–protein interaction analysis. Frames with suitable attacking distances for both nucleophilic attack and proton transfer within the catalytic center were also selected from the modeled trajectory and used for steered MD (sMD) study. In sMD simulation, the catalytic center including side chains of key residues surrounded by the binding ligand NIC-4/4-NPA (Leu97, Gly142, Gly143, Val146, Ser221, Leu304, Ile359, Leu363, Met364, Phe426, and His468 for the NIC-4_hCE1 system; Ala93, Leu97, Gly142, Gly143, Val146, Ser221, Leu255, Leu304, Ile359, Met364, Phe426, and His468 for the 4-NPA_hCE1 system) and the complete structure of NIC-4/4-NPA was described with the semiempirical QM mechanics as the self-consistent charge density functional tight binding method (SCC-DFTB).⁵⁹ The remaining part of each system was treated by the Amber ff14SB force field. The reaction coordinate was set as the distance from nucleophile oxygen OSer221 from the hydroxyl group of Ser221 to the carbonyl carbon CLigand in the carboxyl group of 4-NPA and the amide group of NIC-4, representing the nucleophilic attack process from Ser221. The reaction coordinate was varied from ~2.7 to 1.4 Å with the force constant set to be 200.0 kcal/mol/Å² in 100 ps run. Sampling for the reaction coordinate was dumped every 0.1 ps. The MD simulations were executed under periodic boundary conditions with a 2 fs time step. Van der Waals and short-range electrostatic interactions were estimated within a 10 Å cutoff. The long-range electrostatic interactions were assessed with the particle mesh Ewald method.⁶⁰ The SHAKE algorithm⁶¹ was applied to all bonds including hydrogen atoms.

Immunofluorescence Staining and NIC Costaining in Fixed Cells. Immunofluorescence analysis of hCE1 was performed using HL7402 cells. The cells in 35 mm × 12 mm glass bottom cell culture dishes were set at a density of 2.5 × 10⁵ /mL. The cells were fixed with 100% methanol (chilled at −20 °C) at room temperature for 5 min, permeabilized with 0.1% Triton X-100 for 10 min, blocked with 1% BSA for 1 h, and labeled with 2 µg/mL Rabbit primary antibody for 3 h at room temperature. NIC-4 and NIC-2 were used at a concentration of 5 µM in PBS at room temperature for the hCE1 staining test (blue channel imaging). In another group, the goat antirabbit IgG (H + L) Cross-Adsorbed Secondary Antibody DyLight 488 conjugate was used at a concentration of 2 µg/mL in PBS containing 0.2% BSA for 45 min for the labeling of hCE1 in the cytoplasm (green channel imaging). Nuclei were stained with Nucview Red Live (red channel imaging).

Confocal Fluorescence Imaging. Confocal fluorescence images were observed with an Olympus FV1000 confocal laser-scanning microscope with an objective lens (×100). For the blue channel, the excitation wavelength was set at 405 nm, and blue emission was collected with a 425–475 nm window. For the green channel, the excitation wavelength was set at 488 nm, and green emission was collected with a 500–600 nm window. For the red channel, the excitation wavelength was set at 635 nm, and green emission was collected with a 647–755 nm window.

Long-Term SIM Imaging. LU-NV series laser units (405 nm; 488 nm) are used. Long-term SIM imaging was performed by continuous imaging of dozens of minutes at 20 s intervals after 30 min incubation of NIC-4 with HL7402 cells or cells processed with the immunofluorescent staining procedure. Time-lapse images and time-

colored images are provided to depict the dynamic movement of targeted movement.

ASSOCIATED CONTENT

Supporting Information

The Supporting Information is available free of charge at <https://pubs.acs.org/doi/10.1021/acs.jmedchem.1c01469>.

Detailed experimental and theoretical procedure schemes, equations, supported figures and tables, and synthetic routes and characterizations of C₂₀H₂₁ClN₂O₃, C₁₉H₁₉ClN₂O₄, C₁₉H₁₈N₂O₄, and C₂₀H₂₁ClN₂O₃ (PDF) Formular strings and biochemical data (CSV)

AUTHOR INFORMATION

Corresponding Author

Keli Han – State Key Laboratory of Molecular Reaction Dynamics, Dalian Institute of Chemical Physics, Chinese Academy of Sciences (CAS), Dalian 116023, China; Institute of Molecular Sciences and Engineering, Shandong University, Qingdao 266237, China;  orcid.org/0000-0001-9239-1827; Email: khan@dicp.ac.cn

Authors

Yan Jia – State Key Laboratory of Molecular Reaction Dynamics, Dalian Institute of Chemical Physics, Chinese Academy of Sciences (CAS), Dalian 116023, China;  orcid.org/0000-0002-0769-4389

Jiayue Wang – Department of Pharmacy, Peking University Shenzhen Hospital, Shenzhen 518036, China; College of Pharmacy, Academy of Integrative Medicine, Dalian Medical University, Dalian 116044, China;  orcid.org/0000-0001-5068-631X

Peng Li – Institute of Molecular Sciences and Engineering, Shandong University, Qingdao 266237, China;  orcid.org/0000-0002-9700-4643

Xiaochi Ma – College of Pharmacy, Academy of Integrative Medicine, Dalian Medical University, Dalian 116044, China;  orcid.org/0000-0003-4397-537X

Complete contact information is available at:
<https://pubs.acs.org/10.1021/acs.jmedchem.1c01469>

Author Contributions

Y.J. and J.W. contributed equally. Y.J. and J.W. carried out the study and wrote the manuscript. Y.J. and P.L. designed the synthetic procedures. X.M. contributed to imaging protocol design and helped to edit the manuscript. K.H. conceived and supervised the research.

Funding

This work was supported by the National Natural Science Foundation of China (grant number 21703245 and 21673237, China Postdoctoral Science Foundation Grant 2020M680957, Project of Shanxi Provincial Health Commission 2020011).

Notes

The authors declare no competing financial interest.

ABBREVIATIONS

4-NPA, 4-nitrophenyl acetate; hCEs, human carboxylesterases; NCEN, reported hCE2 fluorescent probe in ref 41.; R1-NH-CO-R2 and R1-NR2-CO-R3, R1, R2, and R3 in each structure type refer to nonhydrogen and varied substitution groups. R1 in the former type is not equivalent to R1 in the latter one, so as for R2 and R3; SAR, structure–activity relationship; SIM,

structured illumination microscopy; SMI, small molecule inhibitor

■ REFERENCES

- (1) Tang, Y.; Zhao, Y.; Lin, W. Preparation of robust fluorescent probes for tracking endogenous formaldehyde in living cells and mouse tissue slices. *Nat. Protoc.* **2020**, *15*, 3499–3526.
- (2) Zhang, C.; Liu, T.; Su, Y.; Luo, S.; Zhu, Y.; Tan, X.; Fan, S.; Zhang, L.; Zhou, Y.; Cheng, T.; Shi, C. A near-infrared fluorescent heptamethine indocyanine dye with preferential tumor accumulation for in vivo imaging. *Biomaterials* **2010**, *31*, 6612–6617.
- (3) Wang, Y.; Yu, F.; Luo, X.; Li, M.; Zhao, L.; Yu, F. Visualization of carboxylesterase 2 with a near-infrared two-photon fluorescent probe and potential evaluation of its anticancer drug effects in an orthotopic colon carcinoma mice model. *Chem. Commun.* **2020**, *56*, 4412–4415.
- (4) Wang, R.; Han, X.; You, J.; Yu, F.; Chen, L. Ratiometric near-infrared fluorescent probe for synergistic detection of monoamine oxidase B and its contribution to oxidative stress in cell and mice aging models. *Anal. Chem.* **2018**, *90*, 4054–4061.
- (5) Gu, L.; Li, Y.; Zhang, S.; Xue, Y.; Li, W.; Li, D.; Xu, T.; Ji, W. Molecular resolution imaging by repetitive optical selective exposure. *Nat. Methods* **2019**, *16*, 1114–1118.
- (6) Schermelleh, L.; Ferrand, A.; Huser, T.; Eggeling, C.; Sauer, M.; Bielhmaier, O.; Drummen, G. P. C. Super-resolution microscopy demystified. *Nat. Cell Biol.* **2019**, *21*, 72–84.
- (7) Thomas, J. A. Optical imaging probes for biomolecules: an introductory perspective. *Chem. Soc. Rev.* **2015**, *44*, 4494–4500.
- (8) Giepmans, B. N. G.; Adams, S. R.; Ellisman, M. H.; Tsien, R. Y. Review - The fluorescent toolbox for assessing protein location and function. *Science* **2006**, *312*, 217–224.
- (9) Wu, Q.; Jing, Y.; Zhao, T.; Gao, J.; Cai, M.; Xu, H.; Liu, Y.; Liang, F.; Chen, J.; Wang, H. Development of small molecule inhibitor-based fluorescent probes for highly specific super-resolution imaging. *Nanoscale* **2020**, *12*, 21591–21598.
- (10) Miller, L. W.; Cornish, V. W. Selective chemical labeling of proteins in living cells. *Curr. Opin. Chem. Biol.* **2005**, *9*, 56–61.
- (11) Gronemeyer, T.; Godin, G.; Johnsson, K. Adding value to fusion proteins through covalent labelling. *Curr. Opin. Biotechnol.* **2005**, *16*, 453–458.
- (12) Ries, J.; Kaplan, C.; Platonova, E.; Eghlidi, H.; Ewers, H. A simple, versatile method for GFP-based super-resolution microscopy via nanobodies. *Nat. Methods* **2012**, *9*, 582–584.
- (13) Opazo, F.; Levy, M.; Byrom, M.; Schäfer, C.; Geisler, C.; Groemer, T. W.; Ellington, A. D.; Rizzoli, S. O. Aptamers as potential tools for super-resolution microscopy. *Nat. Methods* **2012**, *9*, 938–939.
- (14) Song, X.; Han, X.; Yu, F.; Zhang, X.; Chen, L.; Lv, C. Polyamine-targeting gefitinib prodrug and its near-infrared fluorescent theranostic derivative for monitoring drug delivery and lung cancer therapy. *Theranostics* **2018**, *8*, 2217–2228.
- (15) Jing, Y.; Cai, M.; Zhou, L.; Jiang, J.; Gao, J.; Wang, H. Application of an inhibitor-based probe to reveal the distribution of membrane PSMA in dSTORM imaging. *Chem. Commun.* **2020**, *56*, 13241–13244.
- (16) Lee, J.-S.; Kim, Y. K.; Vendrell, M.; Chang, Y.-T. Diversity-oriented fluorescence library approach for the discovery of sensors and probes. *Mol. BioSyst.* **2009**, *5*, 411–421.
- (17) Son, J.; Lee, J.-J.; Lee, J.-S.; Schüller, A.; Chang, Y.-T. Isozyme-specific fluorescent inhibitor of glutathione S-transferase omega 1. *ACS Chem. Biol.* **2010**, *5*, 449–453.
- (18) Macalino, S. J.; Gosu, V.; Hong, S.; Choi, S. Role of computer-aided drug design in modern drug discovery. *Arch. Pharm. Res.* **2015**, *38*, 1686–1701.
- (19) Satoh, T.; Hosokawa, M. The mammalian carboxylesterases: From molecules to functions. *Annu. Rev. Pharmacol.* **1998**, *38*, 257–288.
- (20) Crow, J. A.; Middleton, B. L.; Borazjani, A.; Hatfield, M. J.; Potter, P. M.; Ross, M. K. Inhibition of carboxylesterase 1 is associated with cholestrylo ester retention in human THP-1 monocyte/macrophages. *Biochim. Biophys. Acta* **2008**, *1781*, 643–654.
- (21) Hosokawa, M. Structure and catalytic properties of carboxylesterase isozymes involved in metabolic activation of prodrugs. *Molecules* **2008**, *13*, 412–431.
- (22) Xu, G.; Zhang, W.; Ma, M. K.; McLeod, H. L. Human carboxylesterase 2 is commonly expressed in tumor tissue and is correlated with activation of irinotecan. *Clin. Cancer Res.* **2002**, *8*, 2605–2611.
- (23) Pratt, S. E.; Durland-Busbice, S.; Shepard, R. L.; Heinz-Taheny, K.; Iversen, P. W.; Dantzig, A. H. Human carboxylesterase-2 hydrolyzes the prodrug of gemcitabine (LY2334737) and confers prodrug sensitivity to cancer cells. *Clin. Cancer Res.* **2013**, *19*, 1159–1168.
- (24) Dominguez, E.; Galmozzi, A.; Chang, J. W.; Hsu, K. L.; Pawlak, J.; Li, W.; Godio, C.; Thomas, J.; Partida, D.; Niessen, S.; O'Brien, P. E.; Russell, A. P.; Watt, M. J.; Nomura, D. K.; Cravatt, B. F.; Saez, E. Integrated phenotypic and activity-based profiling links Ces3 to obesity and diabetes. *Nat. Chem. Biol.* **2014**, *10*, 113–121.
- (25) Hatfield, M. J.; Potter, P. M. Carboxylesterase inhibitors. *Expert Opin. Ther. Pat.* **2011**, *21*, 1159–1171.
- (26) Wadkins, R. M.; Hyatt, J. L.; Yoon, K. J. P.; Morton, C. L.; Lee, R. E.; Damodaran, K.; Beroza, P.; Danks, M. K.; Potter, P. M. Discovery of novel selective inhibitors of human intestinal carboxylesterase for the amelioration of irinotecan-induced diarrhea: Synthesis, quantitative structure-activity relationship analysis, and biological activity. *Mol. Pharmacol.* **2004**, *65*, 1336–1343.
- (27) Umehara, K. I.; Zollinger, M.; Kigondu, E.; Witschi, M.; Juif, C.; Huth, F.; Schiller, H.; Chibale, K.; Camenisch, G. Esterase phenotyping in human liver *in vitro*: specificity of carboxylesterase inhibitors. *Xenobiotica* **2016**, *46*, 862–867.
- (28) Binder, R. J.; Hatfield, M. J.; Chi, L. Y.; Potter, P. M. Facile synthesis of 1,2-dione-containing abietane analogues for the generation of human carboxylesterase inhibitors. *Eur. J. Med. Chem.* **2018**, *149*, 79–89.
- (29) Abzianidze, V. V.; Prokofieva, D. S.; Beltyukov, P. P.; Kuznetsov, V. A.; Bogachenkov, A. S.; Rodygin, K. S. Phosphorylated flavonoids as selective carboxylesterase inhibitors. *Mendeleev Commun.* **2019**, *29*, 61–63.
- (30) Wang, D. D.; Zou, L. W.; Jin, Q.; Hou, J.; Ge, G. B.; Yang, L. Recent progress in the discovery of natural inhibitors against human carboxylesterases. *Fitoterapia* **2017**, *117*, 84–95.
- (31) Satoh, T.; Hosokawa, M. Structure, function and regulation of carboxylesterases. *Chem.-Biol. Interact.* **2006**, *162*, 195–211.
- (32) Hosokawa, M.; Furihata, T.; Yaginuma, Y.; Yamamoto, N.; Koyano, N.; Fujii, A.; Nagahara, Y.; Satoh, T.; Chiba, K. Genomic structure and transcriptional regulation of the rat, mouse, and human carboxylesterase genes. *Drug Metab. Rev.* **2007**, *39*, 1–15.
- (33) Bencharit, S.; Edwards, C. C.; Morton, C. L.; Howard-Williams, E. L.; Kuhn, P.; Potter, P. M.; Redinbo, M. R. Multisite promiscuity in the processing of endogenous substrates by human carboxylesterase 1. *J. Mol. Biol.* **2006**, *363*, 201–214.
- (34) Bencharit, S.; Morton, C. L.; Howard-Williams, E. L.; Danks, M. K.; Potter, P. M.; Redinbo, M. R. Structural insights into CPT-11 activation by mammalian carboxylesterases. *Nat. Struct. Biol.* **2002**, *9*, 337–342.
- (35) Crow, J. A.; Herring, K. L.; Xie, S. Q.; Borazjani, A.; Potter, P. M.; Ross, M. K. Inhibition of carboxylesterase activity of THP1 monocytes/macrophages and recombinant human carboxylesterase 1 by oxysterols and fatty acids. *Biochim. Biophys. Acta* **2010**, *1801*, 31–41.
- (36) Hatfield, M. J.; Tsurkan, L. G.; Hyatt, J. L.; Edwards, C. C.; Lemoff, A.; Jeffries, C.; Yan, B.; Potter, P. M. Modulation of esterified drug metabolism by tanshinones from *Salvia miltiorrhiza* ("Danshen"). *J. Nat. Prod.* **2013**, *76*, 36–44.
- (37) Hill, R. A.; Connolly, J. D. Triterpenoids. *Nat. Prod. Rep.* **2015**, *32*, 273–327.

- (38) Wadkins, R. M.; Hyatt, J. L.; Edwards, C. C.; Tsurkan, L.; Redinbo, M. R.; Wheelock, C. E.; Jones, P. D.; Hammock, B. D.; Potter, P. M. Analysis of mammalian carboxylesterase inhibition by trifluoromethylketone-containing compounds. *Mol. Pharmacol.* **2007**, *71*, 713–723.
- (39) Hyatt, J. L.; Tsurkan, L.; Wierdl, M.; Edwards, C. C.; Danks, M. K.; Potter, P. M. Intracellular inhibition of carboxylesterases by benzil: modulation of CPT-11 cytotoxicity. *Mol. Cancer Ther.* **2006**, *5*, 2281–2288.
- (40) Higuchi, R.; Fukami, T.; Nakajima, M.; Yokoi, T. Prilocaine- and lidocaine-induced methemoglobinemia is caused by human carboxylesterase-, CYP2E1-, and CYP3A4-mediated metabolic activation. *Drug Metab. Dispos.* **2013**, *41*, 1220–1230.
- (41) Jin, Q.; Feng, L.; Wang, D. D.; Dai, Z. R.; Wang, P.; Zou, L. W.; Liu, Z. H.; Wang, J. Y.; Yu, Y.; Ge, G. B.; Cui, J. N.; Yang, L. A two-photon ratiometric fluorescent probe for imaging carboxylesterase 2 in living cells and tissues. *ACS Appl. Mater. Interfaces* **2015**, *7*, 28474–28481.
- (42) Quinney, S. K.; Sanghani, S. P.; Davis, W. I.; Hurley, T. D.; Sun, Z.; Murry, D. J.; Bosron, W. F. Hydrolysis of capecitabine to 5'-deoxy-5-fluorocytidine by human carboxylesterases and inhibition by loperamide. *J. Pharmacol. Exp. Ther.* **2005**, *313*, 1011–1016.
- (43) Zou, L. W.; Jin, Q.; Wang, D. D.; Qian, Q. K.; Hao, D. C.; Ge, G. B.; Yang, L. Carboxylesterase inhibitors: an update. *Curr. Med. Chem.* **2018**, *25*, 1627–1649.
- (44) Hakamata, W.; Tamura, S.; Hirano, T.; Nishio, T. Multicolor imaging of endoplasmic reticulum-located esterase as a prodrug activation enzyme. *ACS Med. Chem. Lett.* **2014**, *5*, 321–325.
- (45) Tian, Z.; Ding, L.; Li, K.; Song, Y.; Dou, T.; Hou, J.; Tian, X.; Feng, L.; Ge, G.; Cui, J. Rational design of a long-wavelength fluorescent probe for highly selective sensing of carboxylesterase 1 in living systems. *Anal. Chem.* **2019**, *91*, 5638–5645.
- (46) Liu, Z.-M.; Feng, L.; Hou, J.; Lv, X.; Ning, J.; Ge, G.-B.; Wang, K.-W.; Cui, J.-N.; Yang, L. A ratiometric fluorescent sensor for highly selective detection of human carboxylesterase 2 and its application in living cells. *Sens. Actuators B: Chem.* **2014**, *205*, 151–157.
- (47) Olson, M. J.; Martin, J. L.; LaRosa, A. C.; Brady, A. N.; Pohl, L. R. Immunohistochemical localization of carboxylesterase in the nasal mucosa of rats. *J. Histochem. Cytochem.* **1993**, *41*, 307–311.
- (48) Fleming, C. D.; Bencharit, S.; Edwards, C. C.; Hyatt, J. L.; Tsurkan, L.; Bai, F.; Fraga, C.; Morton, C. L.; Howard-Williams, E. L.; Potter, P. M.; Redinbo, M. R. Structural insights into drug processing by human carboxylesterase 1: Tamoxifen, mevastatin, and inhibition by benzil. *J. Mol. Biol.* **2005**, *352*, 165–177.
- (49) Dolinsky, T. J.; Nielsen, J. E.; McCammon, J. A.; Baker, N. A. PDB2PQR: an automated pipeline for the setup of Poisson-Boltzmann electrostatics calculations. *Nucleic Acids Res.* **2004**, *32*, W665–W667.
- (50) Maier, J. A.; Martinez, C.; Kasavajhala, K.; Wickstrom, L.; Hauser, K. E.; Simmerling, C. ff14SB: Improving the accuracy of protein side chain and backbone parameters from ff99SB. *J. Chem. Theory Comput.* **2015**, *11*, 3696–3713.
- (51) Case, D.A., Cerutti, D. S., Cheatham, T. A. D., Duke, R.E., Giese, T.J., Gohlke, H., Goetz, A.W., Greene, D., Homeyer, N., Izadi, S., Kovalenko, A., Lee, T.S., LeGrand, S., Li, P., Lin, C., Liu, J., Luchko, T., Luo, R., Mermelstein, D., Merz, K.M., Monard, G., Nguyen, H., Omelyan, I., Onufriev, A., Pan, F., Qi, R., Roe, D.R., Roitberg, A., Sagui, C., Simmerling, C.L., Botello-Smith, W.M., Swails, J., Walker, R.C., Wang, J., Wolf, R.M., Wu, X., Xiao, L., York, D.M., Kollman, P. A. AMBER 16. 2017.
- (52) Lee, C. T.; Yang, W. T.; Parr, R. G. Development of the colle-salvetti correlation-energy formula into a functional of the electron-density. *Phys. Rev. B* **1988**, *37*, 785–789.
- (53) Becke, A. D. Density-functional thermochemistry .1. The effect of the exchange-only gradient correction. *J. Chem. Phys.* **1992**, *96*, 2155–2160.
- (54) Becke, A. D. Density-functional thermochemistry .3. The role of exact exchange. *J. Chem. Phys.* **1993**, *98*, 5648–5652.
- (55) Ditchfield, R.; Hehre, W. J.; Pople, J. A. Self-Consistent Molecular-Orbital Methods .9. Extended gaussian-type basis for molecular-orbital studies of organic molecules. *J. Chem. Phys.* **1971**, *54*, 724–728.
- (56) Frisch, M. J.; Trucks, G. W.; Schlegel, H. B.; Scuseria, G. E.; Robb, M. A.; Cheeseman, J. R.; Scalmani, G.; Barone, V.; Petersson, G. A.; Nakatsuji, H.; Li, X.; Caricato, M.; Marenich, A. V.; Bloino, J.; Janesko, B. G.; Gomperts, R.; Mennucci, B.; Hratchian, H. P.; Ortiz, J. V.; Izmaylov, A. F.; Sonnenberg, J. L.; Williams-Young, D.; Ding, F.; Lipparini, F.; Egidi, F.; Goings, J.; Peng, B.; Petrone, A.; Henderson, T.; Ranasinghe, D.; Zakrzewski, V. G.; Gao, J.; Rega, N.; Zheng, G.; Liang, W.; Hada, M.; Ehara, M.; Toyota, K.; Fukuda, R.; Hasegawa, J.; Ishida, M.; Nakajima, T.; Honda, Y.; Kitao, O.; Nakai, H.; Vreven, T.; Throssell, K.; Montgomery, Jr., J. A.; Peralta, J. E.; Ogliaro, F.; Bearpark, M. J.; Heyd, J. J.; Brothers, E. N.; Kudin, K. N.; Staroverov, V. N.; Keith, T. A.; Kobayashi, R.; Normand, J.; Raghavachari, K.; Rendell, A. P.; Burant, J. C.; Iyengar, S. S.; Tomasi, J.; Cossi, M.; Millam, J. M.; Klene, M.; Adamo, C.; Cammi, R.; Ochterski, J. W.; Martin, R. L.; Morokuma, K.; Farkas, O.; Foresman, J. B.; Fox, D. J. *Gaussian 16, Revision A 03*; Gaussian, Inc.: Wallingford CT, 2016.
- (57) Trott, O.; Olson, A. J. Software news and update AutoDock Vina: Improving the speed and accuracy of docking with a new scoring function, efficient optimization, and multithreading. *J. Comput. Chem.* **2009**, *31*, 455–461.
- (58) Jorgensen, W. L.; Chandrasekhar, J.; Madura, J. D.; Impey, R. W.; Klein, M. L. Comparison of simple potential functions for simulating liquid water. *J. Chem. Phys.* **1983**, *79*, 926–935.
- (59) Gaus, M.; Goez, A.; Elstner, M. Parametrization and benchmark of DFTB3 for organic molecules. *J. Chem. Theory Comput.* **2013**, *9*, 338–354.
- (60) Essmann, U.; Perera, L.; Berkowitz, M. L.; Darden, T.; Lee, H.; Pedersen, L. G. A smooth particle mesh ewald method. *J. Chem. Phys.* **1995**, *103*, 8577–8593.
- (61) Ryckaert, J. P.; Cicotti, G.; Berendsen, H. J. C. Numerical-integration of cartesian equations of motion of a system with constraints - molecular-dynamics of N-Alkanes. *J. Comput. Phys.* **1977**, *23*, 327–341.